

# Electrode-assisted trapping and release of droplets on hydrophilic patches in a hydrophobic microchannel

Arjen M. Pit<sup>1</sup>  · Sander Bonestroo<sup>1</sup> · Daniel Wijnperlé<sup>1</sup> · Michèl H. G. Duits<sup>1</sup> · Frieder Mugele<sup>1</sup>

Received: 31 May 2016 / Accepted: 5 August 2016 / Published online: 16 August 2016  
© The Author(s) 2016. This article is published with open access at Springerlink.com

**Abstract** In two-phase flow microfluidics, there is an increasing interest in technologies which enable the encapsulation of biological cells into aqueous drops and the subsequent study of their molecular (excretion or lysis) products. One not yet available but very promising analysis method is the use of biospecific surface patches embedded in the wall of microfluidic channels. In this paper, we tackle some technological challenges encountered in the development of such applications. In the detection protocol, each drop must be enabled to wet the designated patch, be held in contact long enough for biomolecular detection and subsequently be released. This is engineered via a combination of well-defined chemical sites in the walls of the flow channel and insulated microelectrodes. The tunability of the local electric field allows to modify the competition between chemical (pinning) forces which tend to immobilize the drop and hydrodynamic forces which oppose this process. We developed a prototype microfluidic device which offers this functionality. A channel structure is sandwiched between an actuation surface with electrowetting (EW) electrodes on one side and a detector surface with

a hydrophilic patch amidst a hydrophobic environment on the other. Two pairs of carefully aligned EW electrodes are used: one for drop adherence and another one for the subsequent release. We demonstrate these operations and discuss the required voltage signals in terms of the forces on the drop. Finally, we discuss possible steps for further improvement in the device.

**Keywords** Microfluidics · Wetting · Electrowetting · Lab-on-a-chip · Lab-in-a-drop

## 1 Introduction

Microfluidics—in particular droplet-based microfluidics—has become a very popular tool since its advent in the 1980s. Advantages include miniaturization, parallelization and compartmentalization, which—together with high speeds and the ability of upscaling—result in cost reduction and enable the use of statistical analysis (Casadevall i Solvas and deMello 2011; Seemann et al. 2012). Great examples of the use of microfluidics are large-quantity emulsification (in food processing), inkjet printing and whole genome sequencing. (Calvert 2001; Margulies et al. 2005; Nisisako and Torii 2008).

One of the key application areas in microfluidics is biomedical diagnostics (Guo et al. 2012; Song et al. 2006; Theberge et al. 2010). In this field, challenges arise in combining material properties with biochemical molecules and in the detection of small quantities of analyte in complex samples. In particular, the analysis of individual cells has become a topic of interest (Takinoue and Takeuchi 2011).

The most common detection techniques are optical or electrical (Erickson et al. 2008; Kuswandi et al. 2007). The dominant technique remains the fluorescence assay.

---

**Electronic supplementary material** The online version of this article (doi:10.1007/s10404-016-1789-z) contains supplementary material, which is available to authorized users.

---

✉ Michèl H. G. Duits  
m.h.g.duits@utwente.nl

Arjen M. Pit  
a.m.pit@utwente.nl

Frieder Mugele  
f.mugele@utwente.nl

<sup>1</sup> Physics of Complex Fluids Group, MESA+ Institute, University of Twente, P.O. Box 217, 7500 AE Enschede, The Netherlands

However, the need to label with (large) fluorescent molecules can influence the chemical process under analysis. For this reason, several non-labeling techniques for affinity-based pathogen sensing have been developed (Mairhofer et al. 2009). One of these techniques is surface plasmon resonance imaging (SPRi). SPRi measures the change in refractive index which occurs when antigens from the water phase specifically bind to antibodies which are printed on gold (Rich and Myszkowski 2007; Stojanovic et al. 2014).

Continuous water flow SPRi has been proven capable of detecting and quantifying excreted molecules from single cancer cells over a period of 10 h (Stojanovic et al. 2015). For practical application, it is preferable to do the analysis in a shorter time. The problem here is the dilution of the analyte in the fluid phase. This implies that, by using microfluidics to create small droplets (<100 pL), SPRi could be capable of quickly measuring the excreted proteins of individual cancer cells.

While conventionally used for continuous flow measurements, SPR has previously been combined with droplet microfluidics. One thing must be noted: by using protocols involving individual droplets that have to perform complicated tasks, a manipulation method is required. Many methods have been developed (Chen and Jiang 2012; Cho et al. 2003; Pit et al. 2015b). For combination with SPR, pneumatic membrane valves (Luo et al. 2008) and electrowetting-on-dielectric (EWOD) (Malic et al. 2009, 2011) have been used.

A key obstacle for the further development of these promising droplet-based SPR experiments is that once the aqueous droplet interacts with the (hydrophilic) biomolecules on the substrate, the pinning force may be so strong that the droplet cannot be removed again. This issue has so far been mitigated by using relatively large droplets compared to the hydrophilic patch size. When using 100-pL droplets, however, and keeping in mind that the technique of SPRi requires gold patches to be at least in the order of tens of microns (Yeatman 1996), the size of patch and droplet is practically equal. This underlines that important cases exist, in which the problem of the strong pinning force cannot be circumvented by using larger droplets; another strategy is needed.

We are particularly interested in the combination of droplet-based microfluidics with SPRi for diagnosis of various excreted products of an individual cancer cell, while the droplet is still in flow. Key challenges are: (1) droplets have to be held in place at a detection site long enough for analysis and (2) they have to be released and transported to the next measurement site. For the trapping of droplets, passive (Bithi et al. 2014; Fradet et al. 2011) and active (de Ruiter et al. 2014; Leung et al. 2012) methods have been developed. For active release, the options are mainly restricted to using higher flow rates, of which the pressure

changes can be impractical, e.g., for droplet generation, in microfluidic chips.

In this paper, we explore a new method for controlling both the adherence and the detachment of droplets on designated hydrophilic patches inside a microfluidic chip. Here, the droplets are in the pL size regime, and ambient oil is used to isolate and transport the droplets. These design aspects are very well suited for applications with individual cells in drops; not only are the dimensions in the proper range, but also the use of an oil flow meets the practical requirements very well: Droplets can be generated and sorted at high rates (Baret et al. 2009; Pit et al. 2015a; Schmid et al. 2014), and both losses of water and biomolecules to the environment are minimized. This high-speed droplet generation and screening are, for instance, required for isolating circulating tumor cells, of which a patient has very few.

The key novelty is the design of a multifunctional chip that contains hydrophilic patches amidst a hydrophobic environment and two sets of insulated electrowetting electrodes for drop manipulation. Multiple challenges were overcome with regard to fabrication, material properties, alignment and sealing. Several micro- and macro-fabrication techniques are combined and developed, which are explained in detail.

Besides the design and fabrication of the chip, the theory of the relevant forces is described. The forces are calculated and compared to experiments involving the trapping of droplets, the pinning of a droplet to the hydrophilic patch and the subsequent release from the patch by the secondary electrode pair.

## 2 Device concept

Our final, envisioned device will incorporate a drop generator, cell sorter (Pit et al. 2015a) and various storage and detection arrays, as shown in de Ruiter et al. (2014). Here, we focus on overcoming the difficulties that result from working with wetting defects. The principal features of our method are illustrated in Fig. 1. Each pair of EW electrodes separated by a narrow gap serves as an energy well for the aqueous drop, where the depth of the well (or equivalently the attractive force) can be controlled via the voltage difference between the two. When properly designed, droplets can be manipulated by the electrodes without the need to change the oil flow rate.

Two key issues have to be addressed:

1. The thin oil film between droplet and channel wall

A stationary droplet in oil will wet a substrate to obtain an equilibrium contact angle. However, when a droplet

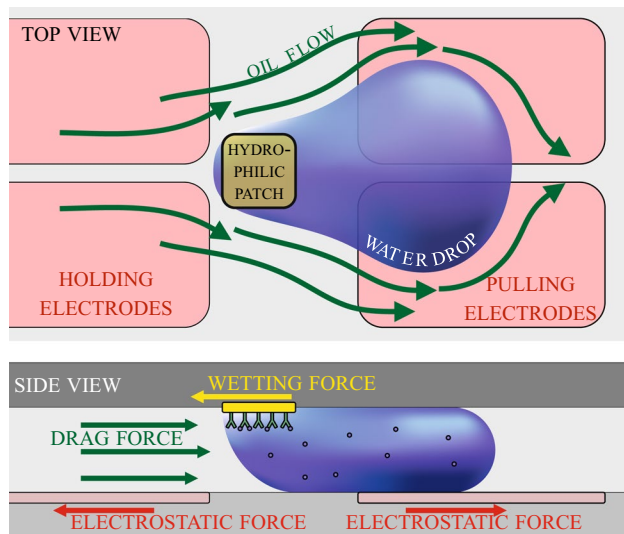


**Fig. 1** Schematic overview of the desired functionality of a microchip where a droplet interacts with an antibody-covered gold patch while in oil flow and with electrodes for holding a drop, and pulling it off

flows in oil (in an oil-wetting channel), a thin oil film is present between the droplet and the wall. This means that a droplet flowing over a hydrophilic patch will be lubricated by a thick oil film. It will most likely not feel the presence of that patch and pass without being trapped. We therefore use a pair of electrowetting electrodes to trap the droplet above the patch until the oil film breaks up.

2. The competition between electrowetting, pinning and drag forces

Before the oil film can break up, the droplet first has to be trapped above the patch. Therefore, the electrowetting (trapping) force will have to be stronger than the viscous drag force due to the flowing oil. Once the droplet has spread over the hydrophilic patch, the pinning force has to be stronger than the drag force. In this way, the droplet can be passively held in place. Finally, to remove the droplet from the patch, the combination of electrowetting pulling (by activating the electrodes downstream of the patch) and the drag force together need to exceed the pinning force to release the drop (see Fig. 1).

For creating a microfluidic prototype, we focus on solving the aforementioned issues. We have previously shown that electrodes are capable of trapping droplets in oil flow (de Ruiter et al. 2014), and thus, it makes sense to use electrodes as the active force for holding a droplet in flow, until it wets the hydrophilic patch. Likewise, a second pair of pulling electrodes (together with the oil drag) should be capable of pulling the pinned droplet off the patch.

## 3 Materials and methods

### 3.1 Motivation of design choices

A thin oil film between electrode and droplet can actively be broken up using electrowetting (Staicu and Mugele 2006). However, SPR requires a flat substrate with few refractive index changes. It is preferred to apply gold (and chromium) directly to glass, without a layer of electrodes, insulator, or hydrophobicity in between or on top. For this reason, it was decided to make a two-sided microchip and to make the two-sided modular. The actuation chip half contains the electrode geometries aligned to a thin slab of PDMS, which forms the (open) microchannel and simultaneously functions as the insulating layer required for electrowetting. The sensing chip half consists of a hydrophobized glass slide with inlets and small hydrophilic gold patches, which resemble printed antibodies as used in SPRi.

This modularity increases the universality of our microfluidic device, where the two chip halves are individually replaceable. Modularity also makes integration of the electrode and open-channel chip with other existing diagnostic tools easier. Changing from a one-sided to a two-sided device does, however, require a completely new fabrication protocol. Instead of attaching a PDMS channel to electrodes already insulated by PDMS (Pit et al. 2015a), we now create a thin slab of PDMS functioning as microchannel and insulator in one. This slab is directly spun, aligned and cured atop the electrode structure, as explained in the following sections.

Eventually, a fabrication protocol was developed that incorporates all the chip requirements and results in nearly perfect chip alignment without failure.

### 3.2 Materials

An overview of the microfluidic device is given in Fig. 4. Upstream, a flow focusing device (FFD) allows for continuous or on-demand generation of droplets. The water phase is phosphate-buffered saline (PBS,  $\sigma = 15$  mS/cm). The continuous phase, controlled by a syringe pump, is light mineral oil ( $\mu = 31.5$  mPas), which wets both the PDMS and Cytosol well. By applying a controlled pressure pulse (voltage, duration) to the water phase, it is possible to create droplets on demand with a radius ranging from 15 to 40  $\mu\text{m}$ . Applying a continuous higher pressure allows to generate uniform droplets continuously at 0–300 Hz rates.

The electrode geometry consists of only three large electrodes of which one is grounded, and the other two can be grounded or active (see Fig. 4d and Online Resource 1). These three electrodes form five consecutive areas where

a droplet can be trapped and released. Each structure has two functions. The first electrode pair is designed for temporarily trapping the droplet. The second electrode pair is designed for release of the droplet from the hydrophilic patch.

The gold patches are located with the same pitch as between the electrode structures and at the same distance from the inlets. Since the powder-blasted inlets are  $\sim 500 \mu\text{m}$  in diameter, this allows plenty of error for the final alignment of the gold patches to the electrode geometry, which does have to be precise.

### 3.3 Electrowetting actuation surface (fabrication)

The actuation chip half consists of a glass substrate with ITO-patterned electrodes, a PDMS insulating layer and microchannel. The fabrication process is schematically shown in Fig. 2. Firstly, the mold for the channel is created.

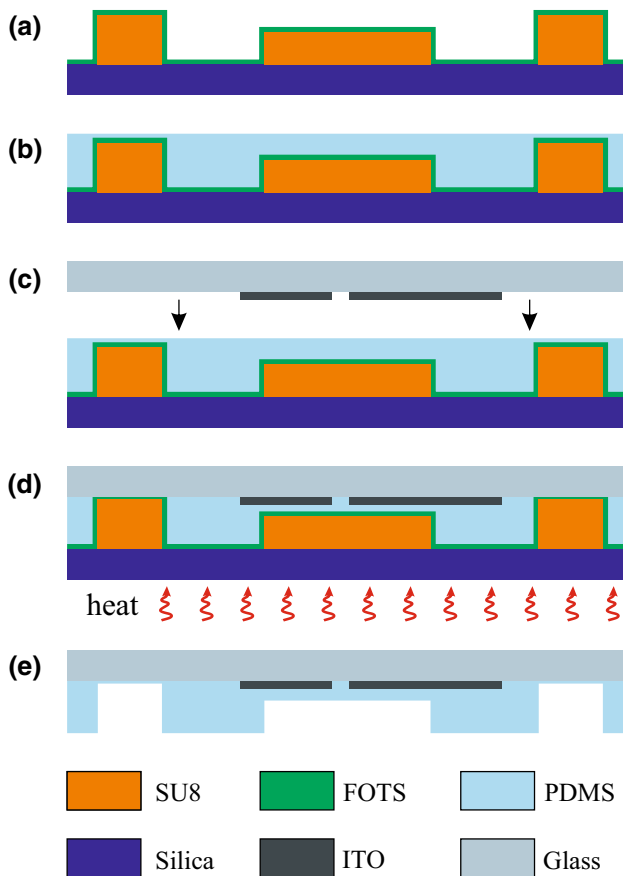


**Fig. 2** Fabrication steps of first chip half. **a** Start with hydrophobized SU8 channel mold atop silica. **b** Spin slight excess of PDMS over channel and pillars. **c** Align ITO electrodes with the channel and press together. **d** Use Peltier element to cure PDMS at  $70^\circ$  for 2 h. **e** Remove the mold to be left with ITO electrodes, covered by a  $\sim 3 \mu\text{m}$  dielectric layer and perfectly aligned in the center of the PDMS channel

A  $52 \mu\text{m}$  layer of SU8 is spun over a silica wafer. Using standard photolithography, the shape of the inversed channel surrounded by support pillars is soft-baked, exposed to UV and cross-linked. Before dissolving the uncured SU8, a secondary layer of  $3 \mu\text{m}$  SU8 is spun over the first layer. For this second layer, only the pillar structures next to the channel are exposed and cross-linked. After developing the uncured SU8, a mold is left with a  $52\text{-}\mu\text{m}$  high channel structure surrounded by support pillars that are  $3 \mu\text{m}$  higher. The mold is then coated with a monolayer of FOTS by vapor deposition under vacuum. This ensures hydrophobicity and facilitates easy removal of the cured PDMS layer from the following process steps.

Next, a  $58\text{-}\mu\text{m}$  layer of PDMS with 10:1 PDMS:curing agent (Sylgard 186) ratio is spun over the mold ensuring a slight excess of PDMS covering the channel and pillars. Using a homebuilt stereomicroscope, which includes 2 translational stages ( $x$ ,  $y$ ,  $z$ ), 1 rotational stage and vacuum suction to hold both the upper and lower substrate in place, the PDMS-covered mold is placed atop a Peltier element on the microscope and is subsequently aligned to a substrate with patterned ITO electrodes. The ITO pattern contains—besides the electrowetting electrodes—alignment markers which follow the exact shape of the channel to aid in the alignment process (see Online Resource 1a).

The Peltier element, mold and electrodes are pressed together on the stereomicroscope, taking care not to encapsulate air bubbles in the corners of the microchannel. Since the PDMS is still liquid, an accidental imperfect alignment can still be corrected by simply moving the translational

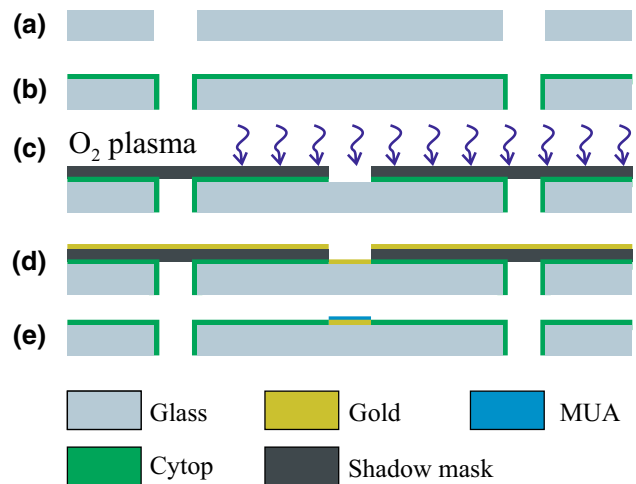


**Fig. 3** Fabrication steps of second chip half. **a** Start with glass slide with powder-blasted inlets. **b** Spin and cure  $1 \mu\text{m}$  of Cytop. **c** Use shadow mask to burn away patches of Cytop with  $\text{O}_2$  plasma. **d** Sputter gold. **e** Remove mask and place substrate in 2 % 11-mercaptoundecanol (MUA) to hydrophilize the gold patches. Rinse with ethanol to remove excess MUA and be left with a hydrophobic substrate with hydrophilic gold patches

and rotational stages of the alignment microscope. Lodged on the microscope, the Peltier is now set to 70 °C for 2 h to ensure the PDMS is fully cured. Since the PDMS bonds covalently to the glass and ITO electrodes, whereas the mold is coated with FOTS, the two substrates are effortlessly separated after curing, allowing the mold to be reused. Because the support pillars of the mold around the channel are 3  $\mu\text{m}$  higher than the channel, the electrodes are covered by a 3- $\mu\text{m}$  layer of PDMS, which is needed as insulation for electrowetting. The final actuation chip half consists of a glass substrate with electrode pattern, insulating layer and aligned channel.

### 3.4 Functional patch surface (fabrication)

The sensing chip half consists of a hydrophobized glass substrate with hydrophilized gold patches and comprises access holes for the liquids. The fabrication process is schematically shown in Fig. 3. Firstly, tapered access holes for the water and oil inlets and the outlet are powder-blasted in a glass wafer. The access holes are temporarily closed off by scotch tape, and 1  $\mu\text{m}$  of Cytop is spun on the opposite side. Putting the wafer in the oven at 80 °C for 30 min

ensures the solvent is evaporated. Then, the oven is set to 180 for 90 min, which ensures the glass transition temperature of Cytop is reached, creating a solid hydrophobic layer of homogeneous thickness. The oven is allowed to slowly cool down to room temperature to prevent cracks forming in the Cytop layer. A shadow mask with square holes, created by KOH etching of a silicon wafer, is aligned with the access holes. The glass wafer and shadow mask are placed in a reactive ion etching (RIE) machine where the Cytop is etched by  $\text{O}_2$  plasma at the locations where eventually the hydrophilic patches will be in the microchannel. Then, chromium (5 nm) and gold (100 nm) are sputter-deposited atop the mask. The mask is removed leaving behind  $\sim 45 \times 45 \mu\text{m}$  square patches of gold on glass surrounded by Cytop. The substrate is diced in individual chips. These chips are put in a 1 mM solution of 11-mercaptoundecanol (MUA) in ethanol for 30 min, which creates a covalently bound hydrophilic monolayer on the gold patches. The chips are flushed with ethanol and dried with nitrogen. The final sensing chip half consists of a glass substrate with microfluidic access holes, a completely hydrophobic Cytop coating, except for the gold patches which are coated with a hydrophilic monolayer of MUA.

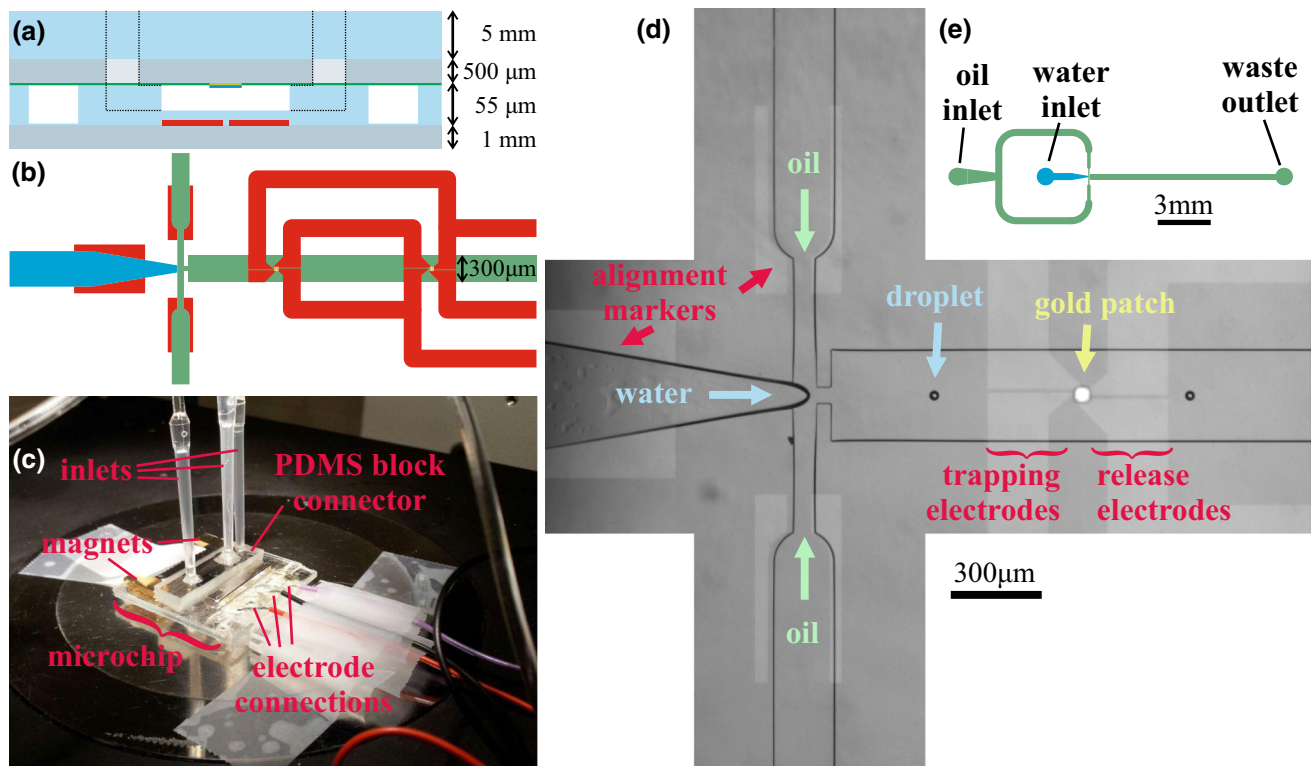


**Fig. 4** **a** Schematic *side view* of the microfluidic chip after alignment of the two chip halves. **b** Overlay of the different mask designs for the microchannel mold (*green, blue*), electrode geometry (*red*) and gold patches (*yellow*). **c** Photograph of the microfluidic chip atop the

microscope. **d** Microscope view of the microchip. **e** Overview of the microchannel design. See Online Resource 1 for all cleanroom masks (color figure online)

### 3.5 Chip assembly

The stereomicroscope is used to align the two chip halves so the hydrophilic gold patches are centered between the trapping and release electrodes. While the connection between PDMS and Cytop provides enough friction to prevent lateral movement after alignment, there is no chemical bonding between the PDMS channel and the Cytop. As an advantage, the chip halves can still be separated and realigned if alignment is not satisfactory. On the other hand, to prevent leaking of the microchannel, neodymium magnets are used on all sides of the microchannel that press the chips together.

For connecting tubing to the inlets, a PDMS block with punched holes is used. The PDMS block and microchip are treated by oxygen plasma for 30 s and then immediately brought together to form a permanent seal. The tubing can be directly pressed into the access holes for a leak-free connection. Finally, electric wiring is glued to the electrode patches using silver glue, as seen in Fig. 4c.

## 4 Theory

In our microfluidic device, there are three important forces acting on the droplets: the electrostatic, drag and pinning force. Estimations of these forces have been presented previously (Cavalli et al. 2015; de Ruiter et al. 2014; t Mannetje et al. 2014), and we give only a short synopsis here.

### 4.1 Electrostatic forces

The electrostatic force, also named electrowetting or dielectrophoretic force, originates from the difference in capacitive energy when the material between two electrodes is displaced by another material with higher permittivity (a larger dielectric constant). In our microfluidic channel, it is a conductive aqueous droplet that displaces the oil, while it spreads over two co-planar electrodes. For simplicity, we ignore the electrostatic energy when oil is between the electrodes. Then, the electrostatic energy that is gained when a conductive droplet displaces the oil is given by the capacitance of, and voltage applied over, the dielectric layer of PDMS atop the electrodes (t Mannetje et al. 2013):

$$E_{\text{el}} = -\frac{1}{2}CU^2 = -\frac{1}{2} \frac{\epsilon_0 \epsilon_r}{d} \frac{A_1 A_2}{A_1 + A_2} U^2 \quad (1)$$

with  $\epsilon_0 \epsilon_r$  the permittivity of PDMS,  $d$  the thickness of the PDMS layer,  $A_1$  and  $A_2$  the position-dependent areas the droplet covers over the grounded and active electrode, and  $U$  the applied potential over the electrodes. The

electrostatic force is the derivative of the change in energy with respect to position, with a maximum given as:

$$F_{\text{el,max}} = -\frac{dE_{\text{el}}}{dx} \approx a \frac{\epsilon_0 \epsilon_r}{d} RU^2 \quad (2)$$

with  $a$  a geometrical factor depending on electrode geometry and  $R$  the droplet radius. The direction of the electrostatic force is as follows: when a droplet covers two electrodes of different potential, the force is directed toward the gap between the electrodes. When a droplet is pushed off the electrodes by, for instance, drag, the electrostatic force will oppose this motion.

### 4.2 Hydrodynamic drag force

The hydrodynamic drag force  $F_d$  on a stationary drop can be estimated by modeling the drop as a (cylindrical) pillar with no-slip boundary conditions in an infinitely wide channel. Since the drop diameter is about one-sixth of the channel width we chose to neglect the effect of the channel walls on the drag force. This yields (de Ruiter et al. 2014):

$$F_d = \left( \frac{24\pi \mu u_{\text{oil}} R^2}{h} \right) \left( 1 + \frac{2K_1(q)}{qK_0(q)} \right) \quad (3)$$

with  $\mu$  the viscosity of the oil,  $u_{\text{oil}}$  its velocity,  $R$  the pillar (i.e., drop) radius,  $h$  the channel height, and  $K_1$  and  $K_2$  modified Bessel functions of the second kind with  $q = 2\sqrt{3}R/h$ . We also assume a constant oil velocity in the center region of the channel.

### 4.3 Pinning force

The pinning force originates from a difference in wettability where a droplet interacts with the substrate. A droplet will prefer to be present on a hydrophilic patch, and thus, a force will be required to remove the droplet from this patch. This force can be estimated as (Cavalli et al. 2015):

$$F_{\text{wet}} = -\gamma_{\text{wo}} \cdot (\cos \theta_{\text{phobic}} - \cos \theta_{\text{philic}}) \cdot \frac{dA_p(x)}{dx} \quad (4)$$

with  $\gamma_{\text{wo}}$  the water–oil interfacial tension ( $\sim 50$  mN/m),  $\theta_{\text{phobic}}$  and  $\theta_{\text{philic}}$  the Young angles on the hydrophobic Cytop, and the hydrophilic patch, respectively, and  $A_p$  the position-dependent area of the droplet overlapping the patch. Assuming the droplet completely covers the entire width of the patch at some point, the maximal pinning force becomes:

$$F_{\text{wet,max}} = \gamma_{\text{wo}} \cdot (\cos \theta_{\text{philic}} - \cos \theta_{\text{phobic}}) \cdot w \quad (5)$$

with  $w$  the width of the patch.

## 5 Results

### 5.1 Droplet trapping

In the first set of experiments, we use a microfluidic device containing the actuation surface but not the patch surface to study the electrostatic trapping of droplets, against the drag force. The oil flow rate is maintained at 400  $\mu\text{L/h}$ , and the water pressure is set to continuously generate droplets of  $R \sim 30 \pm 4 \mu\text{m}$ . The EW voltage  $U$  was increased from 50 to 250  $V_{\text{RMS}}$ , while the AC frequency was kept at 4 kHz. At increasing voltages, droplets are trapped and will coalesce with consecutive droplets (see also Fig. 6a and Online Resource 3) until the hydrodynamic drag force exceeds the trapping force and the droplet is pulled off. The radius  $R^*$  of these droplets was measured downstream of the trapping site and is plotted against  $U^2$  in Fig. 4.

The graph shows that below 130 V, the droplets do not get trapped, although a reduction in the droplet velocity while passing the electrodes is observed. At 140 V, primary droplets are trapped if the electrodes are not yet occupied. When a secondary droplet arrives, an instantaneous coalescence occurs, after which the merged droplet is released. This can be understood from a shift in the force balance: The drag force increases more strongly with increasing drop radius than the electric trapping force. Further raising the voltage from 140 to 190 V, we see a linear increase in

$R^*$  with the (mean) squared voltage. This is in good accordance with the theory, which predicts that the drag force scales as  $R^2$ , while the maximal electrostatic force scales as  $RU^2$ . Since a droplet should be released when  $F_d > F_{\text{el,max}}$ , the slope in the green region  $\frac{R^*}{U^2}$  in Fig. 5 should roughly be constant.

To analyze the force balance in more detail, we calculated the electrostatic and viscous forces for those (coalesced) droplets that are on the brink of being dragged off the electrodes. The drag force was obtained from Eq. (3), by inserting the half width of the (slightly deformed) drop for the radius  $R$ . The electrostatic force was calculated numerically, since the analytic Eq. (2) (right-hand side) considers neither the gap between the electrodes, nor the electrode shape explicitly. Using image analysis, we first extracted the shape of the droplet, the electrode geometry and the areas  $A_1$  and  $A_2$  of the trapped drop on the active and ground electrodes. This allowed to calculate the electrostatic energy from Eq. (1). Then, we determined the local energy landscape, by artificially moving the droplet shape over the electrode geometry (a few pixels back and forth in the flow direction). This enabled us to obtain the electrostatic force (see Online Resource 2), by taking the numerical derivative as in Eq. (2).

The results are presented in Table 1. Even though we should expect the forces to be nearly equal (the drag force should only be slightly favored), it turns out that (for all

**Fig. 5** Radius of the droplets after interaction with the (the first pair of) trapping electrodes at potential  $U$ . The yellow region corresponds to primary droplets passing the electrodes. In the green region, drops are trapped, and consecutive drops coalesce with the trapped droplet until the drag force overcomes the electrostatic force. Also, the actual applied voltage and the average amount of droplets trapped are given for the first four measurements in this region. In the red region (corresponding to EW numbers  $\geq 2.9$ ), saturation occurs, a common observation in electrowetting (color figure online)

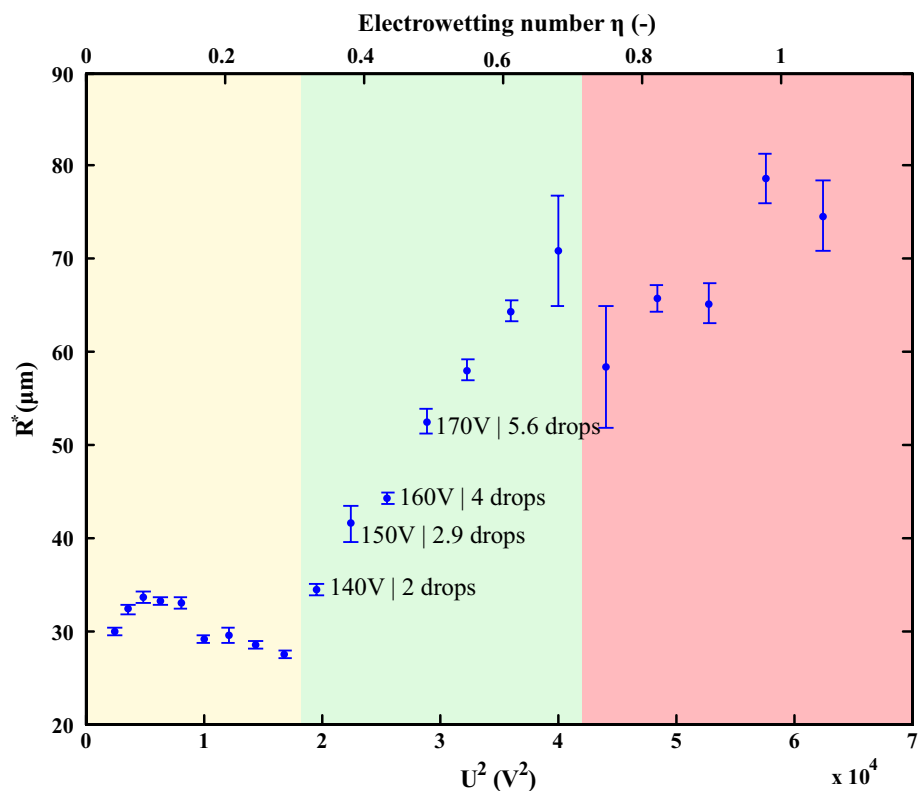


**Table 1** Calculated maximal electrostatic and drag forces on trapped droplets at increasing voltages  $U$  and the corresponding radii  $R$ 

$U$ (V)	$R$ ( $\mu\text{m}$ )	$F_{el}$ ( $\mu\text{N}$ )	$F_{drag}$ ( $\mu\text{N}$ )
140	34	0.85	0.26
150	42	1.4	0.37
160	44	1.6	0.42
170	52	2.2	0.59
180	58	2.3	0.73
190	64	2.9	0.90

four cases) the calculated electrostatic force is a factor 3 larger than the calculated drag force. Given the approximations in the theory and slight errors in input parameters, this systematic deviation is to be expected.

Besides the linearity between  $R^*$  and  $U^2$ , the green region of Fig. 5 also shows the ability to coalesce 2, 3, 4 or 5 droplets at the trapping electrodes. Compared to other methods for electric field-induced merging of droplets (Gu et al. 2011; Schoeman et al. 2014), our technique has two

advantages: The number of coalescing droplets is flexible and can be controlled via the voltage, and the droplets do not need to reach the electrodes simultaneously: The first droplet is simply trapped and waits for the consecutive droplet(s) to merge, after which the final drop is released automatically (see Online Resource 3 and 4).

For voltages above 190 V, a saturation effect is observed: Raising the voltage further does not seem to increase the electrostatic (trapping) force. This is a common occurrence in EW, where the three-phase contact line becomes unstable as the electric field strength increases near the sharp contact angle (Mugele and Baret 2005). Charges— attracted to the interface by the electric field—start repelling each other so strongly that small (charged) satellite droplets are ejected from the mother droplet. This behavior was also observed in our experiments, at voltages above 190 V, and specifically when the droplet was dragged off the electrode (the electric field is strongest at that point). Electrowetting phenomena are generally mapped using the EW number  $\eta = \epsilon_0 \epsilon_r U^2 / 2d\gamma$  (Mugele and Baret 2005), with  $\gamma$  the oil–water interfacial tension (50mN/m). Since

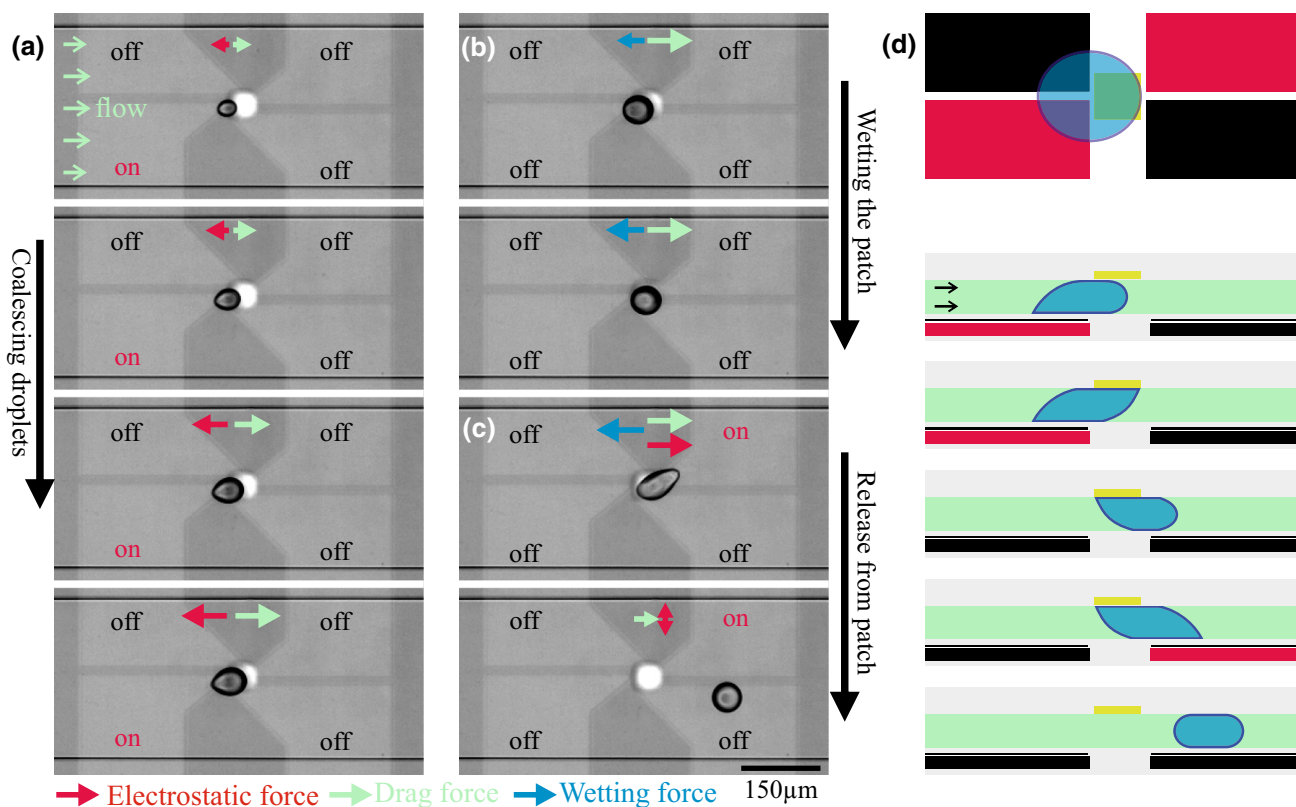


**Fig. 6** Microscopic *top view* of the steps during trapping and release of a droplet on a hydrophilic patch. Oil flow rate (285  $\mu\text{L/h}$ ). **a** Trapping of droplets with electrodes (300 V, 4 kHz). Four consecutive droplets coalesce to form a larger droplet. **b** The electrodes are turned off. The droplet now slowly spreads over the hydrophilic patch. **c** The release electrodes are activated (300 V, 50 Hz), and the droplet is

pulled off the patch. Hereafter, the droplet oscillates at 50 Hz between the electrodes. **d** Schematic representation (*top* and *side views*) of the experiment. In the *side views*, the droplet gets trapped by electrodes, wets the patch, remains adhered to the patch after the trap is switched off and gets pulled off the patch by electrodes. A high-speed video of the experiment can be viewed in Online Resource 6



our geometry uses two co-planar electrodes, it is common to use a correction factor of  $\frac{1}{4}$  in the definition of  $\eta$  to account for the reduced voltage at each electrode contact  $\eta = \epsilon_0 \epsilon_r U^2 / 8d\gamma$ . This quantity is plotted as the upper axis in Fig. 5. The regime where our experimental data level off corresponds to  $\eta \geq 0.7$ . Note, however, that the actual ‘effective’ voltage is higher if the overlap area between the drop and two electrodes is not symmetric (t Mannetje et al. 2014).

Another observation at these high voltages is that wetting defects (locations where droplets tend to adhere without control) are formed in the direct vicinity of the electrodes. Since we did not observe any signs of dielectric breakdown (such as gas bubble formation), we consider it most likely that these defects occur because water is pulled into the porous PDMS layer, displacing oil which previously filled the PDMS.

## 5.2 Droplet wetting the patch

In the following experiments, the two-sided chip as described in Sect. 2 was used, containing electrode structures for EW trapping and release of droplets on one side and hydrophilized gold patches on the other. Droplets of phosphate-buffered saline were generated on demand using pressure pulses. After setting the flow rate of the mineral oil to 285  $\mu\text{L/h}$ , the potential of the trapping electrodes was adjusted to 300  $V_{\text{RMS}}$  to ensure a stable trapping. The requirement of a higher voltage (compared to the trapping experiments in Fig. 5) indicates that the dielectric layer was thicker this time (see our earlier remarks). The AC frequency of the applied voltage signal was 4 kHz.

In the absence of a trapping voltage, the droplets flow past the patch without showing any visible change in shape or velocity (see Online Resource 5). Apparently, the aqueous droplets do not have enough time to ‘sense’ the hydrophilic patch and squeeze out the hydrodynamically entrapped oil. This confirms that the trapping electrodes are needed to force the drop into direct contact with the sensing patch. The electrostatic trapping of droplets proceeds in a similar way as with the other chip: as long as the maximum electrostatic force ( $\propto R$ ) remains larger than the drag force ( $\propto R^2$ ), the generated droplets keep collecting and merging at the trap (see Fig. 6a). Due to the use of pressure pulses, the primary droplets now had a radius  $R \sim 16 \mu\text{m}$ . Up to 7 primary droplets could be collected in this way.

It turned out that for droplets with  $R \sim 32 \mu\text{m}$ , a trapping time of a few seconds was sufficient to achieve wetting of the patch. This was not directly visible on the microscope, but became apparent after grounding both trapping electrodes: The droplet was not picked up by the flow, but did undergo a small downstream displacement. In this process, the droplet slowly increased its coverage of the patch

until it was complete. The droplet then remained stuck to the patch, indicating that the pinning force was larger than the drag force (see Fig. 6b and Online Resource 6).

## 5.3 Droplet pull-off

To detach the drop from the wetted patch, we employed the second set of EW electrodes (situated on the right-hand side of the patch in Fig. 6a). As in the previous experiments, the oil flow rate was kept constant at 285  $\mu\text{L/h}$ . Initially, we applied a similar AC voltage signal as for trapping (300 V, 4 kHz). Here, we observed that, although the droplet did get deformed as the EW force pulled on the droplet, it remained stuck on the patch (not shown). This indicates that the pinning force is so strong that it can even resist the sum of the electrostatic and drag forces.

In most EW applications, the AC frequency is chosen to be high ( $>1$  kHz). This serves to ‘shake’ the contact line of the drop and hence facilitate depinning (Li and Mugele 2008), without causing a vigorous center-of-mass motion. Since the droplets could not get released at 4 kHz, we explored a much lower frequency, expecting that this would result in a mechanical excitation of the entire droplet which was also sufficiently prolonged to allow a large displacement per half cycle. Choosing the frequency well below that of the mechanical droplet resonance retains the advantage of AC signals, while effectively presenting a DC signal: The droplet has enough time to adapt to the slowly changing voltage. This also means that the highest effective voltage is now the peak voltage itself, instead of the RMS voltage, which is  $\sqrt{2}$  times smaller.

Indeed, application of an AC frequency of 50 Hz resulted in stronger deflections of the contact line; close inspection of video frames taken at 7000 fps revealed that the right-hand side contact line of the droplet showed periodic motion in the direction of the activated electrodes. The frequency of this oscillation was 100 Hz, in agreement with expectations: Within each AC cycle, the condition where the two electrodes have the same potential occurs twice. A few cycles were sufficient to release the drop. As a mechanistic explanation, we propose that the sinusoidal deflection of the contact line (see Fig. 6c) at the lower side of the drop is transmitted to the upper side, resulting in depinning from the patch. The release process is also illustrated in Fig. 6d.

Remarkably, just after being released from the patch, the droplet oscillates at 50 Hz between the active and grounded electrodes (see Online Resource 6). Since the EW/DEP electrostatic force depends on the square of the applied potential, it would shake the droplet at 100 Hz. Moreover, this force would tend to center and stretch the droplet, which is also in contradiction with the observations.

Coulomb forces caused by a (positive or negative) net charge of the droplet would produce an alternating motion

at the frequency at which the electrode potentials are switched between positive and negative and thus produce the observed 50 Hz. Since no indications were obtained that the droplets were charged during trapping and pinning, the implication would be that charges are introduced during the interaction with the pull-off electrodes. The formation of charged droplets by EW electrodes is known to occur in scenarios where the droplet is so quickly split into two parts, that the separated (counter) charges residing near the two EW electrodes do not have sufficient time to recombine (Baret and Mugele 2006). Thinking along this line, it might be that during the detaching of the drop, a tiny aqueous volume (too small to observe microscopically) with a residual charge is left behind (with the counter charge residing in the released drop). Another possibility would be that electrically charged satellite droplets are ejected from the main droplet, similar to our observations at high voltages in Sect. 5.1.

For a typical experiment as shown in Fig. 6, the relevant forces can be estimated, using Eqs. (3) and (5) for the drag and pinning forces, and a numerical calculation of the electrostatic force (see Online Resource 2). Additional measurements were done to complete the set of input parameters: a flow velocity  $u_{\text{oil}}$  of 8.5 mm/s (approximated at the centerline of the channel), an oil–water interfacial tension  $\gamma_{\text{ow}}$  of 50 mN/m, a patch width of 45  $\mu\text{m}$  and water contact angles on the Cytop  $\theta_{\text{phobic}}$  of 160° and a receding angle on the MUA  $\theta_{\text{philic}}$  of 50° (see Online Resource 7). This resulted in:

$$F_d \approx 0.33 \mu\text{N}, F_{\text{wet}} \approx 3.6 \mu\text{N}, F_{\text{el,max}} \approx 3.2 \mu\text{N}$$

These numbers, which have to be considered as crude estimates, corroborate that the maximum electrostatic force is larger than the drag force, and that droplets can be trapped with electrodes. Similarly, the pinning force is found to be larger than the drag force, in agreement with our observation that droplets remain on the patch in spite of the flow. Finally, the resultant force of the drag and electrowetting is about as large as the pinning force, explaining the difficulty in removing the droplet from the patch.

## 6 Discussion

### 6.1 Fabrication

In the search for a microfluidic device that contains electrodes as well as hydrophilic patches, many different fabrication protocols have been explored. Finally, we have found a protocol that—with some practice on the experimenter's side—generates a well-aligned, bi-functional, two-sided microchip nearly every time. Several key aspects to this improved fabrication process have to be mentioned. First,

the use of 3- $\mu\text{m}$ -higher pillars around the channel mold automatically ensures the presence of a thin dielectric layer of PDMS atop the electrodes. This simplifies the process and saves time and effort compared to other protocols to create a thin, homogenous dielectric, like separately spinning a PDMS layer, evaporating parylene-c, or dip coating Teflon AF atop the electrodes. Second, since the electrodes and channel are pressed together with liquid PDMS, the mold and electrodes can be moved with respect to each other even after pressing them together. This ensures a near-perfect alignment. Specifically, because, third, the in situ curing of the liquid PDMS by use of a Peltier element on the stereomicroscope ensures that the chip halves do not misalign before curing is complete (for instance, during transport to an oven). Fourth, by using Cytop as a sturdy hydrophobic material for the hydrophilic patch side, instead of, for instance, Teflon AF, it is now possible to use a shadow mask without damaging the hydrophobic layer. This simplifies the local removal of Cytop by oxygen plasma and the sputtering of gold, without the need for additional photolithographic steps. Also, the specific bonding of mercaptoundecanol to gold allows to rinse the Cytop effortlessly, creating a hydrophobic substrate with low contact angle hysteresis around the hydrophilic patches. The elasticity of the 55- $\mu\text{m}$  PDMS layer allows to seal the chip, as long as pressure is applied homogeneously around the channel. For ease of use, in this setup, magnets provided this pressure, which formed a leak-free seal for the oil flow rates and oil type used in this paper.

### 6.2 Operation

As for qualitative functionality, the microchip worked as expected. Trapping electrodes are needed to allow for the passive breakup of the thin oil film and attachment of the droplet to the hydrophilic patch. Even though this process takes less than a few seconds, other applications might require wetting to occur faster. In that case, it would be possible to place the hydrophilic patch on the electrode chip half. The electrostatic force would then actively pull the droplet toward the hydrophilic patch, ensuring an active squeeze-out of the oil film within several milliseconds (Static and Mugele 2006).

After the droplet wets the patch, the pinning force is larger than the drag force, as indicated by the fact that the droplet in flow remains on the patch for prolonged periods of time. This also confirms the need for release electrodes to pull the droplet off the patch.

The trapping/pinning/release experiments were successfully performed multiple times for droplets consisting of 2, 3, 4 and 5 merged primary droplets. Using just one primary droplet only succeeded if the droplet was not given enough time to completely spread over the patch. We can

explain this by the fact that the pinning force for a droplet spread over the patch is determined by the width of the patch (independent of droplet size), while the electrostatic and drag force are determined by the radius of the droplet. Likely due to the non-optimal choice of electrode geometry, it proved to be impossible to drag the droplet from the patch using high-frequency actuation only. The shift to a low-frequency actuation signal finally enabled the release of droplets of radius 19–31  $\mu\text{m}$  from the patch.

The novel functionality of our device has several advantages over previous combinations of electrowetting and SPR. Compared to only using electrowetting for all droplet manipulations (Malic et al. 2009), the addition of two-phase flow microfluidics helps in the release of a droplet from a patch. Furthermore, microfluidics enables the high-speed generation of picoliter-sized droplets (Pit et al. 2015b), which, for instance, can contain single cells (Chabert and Viovy 2008). These small volumes are required to quickly reach sufficient concentrations of cell-excreted molecules inside the droplets to enable SPR detection.

We supply formulas for the estimation of the forces related to our work, which are helpful guidelines for designing a microfluidic chip combining wetting patches and electrowetting.

## 7 Conclusions and outlook

We successfully designed and fabricated a multifunctional, two-sided microchip capable of forcing picoliter-sized droplets to adhere to an artificial wetting defect and thereafter controls the release of the droplet to flow toward a next measurement site. This demonstrates the capability of our technique for future implementation with measurement techniques that require surface molecular interaction.

In the trapping experiments, we observed that the EW and drag forces scale in the expected way with electric field and drop radius. Although quantitative agreement with the used (approximative) theoretical expressions is not achieved, large enough EW trapping forces could be generated, by adapting the voltage to the drop size and flow rate.

Under (our) flow conditions, wetting of the hydrophilic patch by the aqueous drop does not occur spontaneously, even though it is thermodynamically favored. This is ascribed to the presence of an oil film, which does not have sufficient time to be squeezed out. However, using EW forces, it was possible to hold the drop long enough under the patch, for wetting to occur.

The pinning forces from the patch turned out to be strong enough to resist the drag force and hence immobilize the drop. Pull-off from the patch could be achieved with the designated electrodes, however, not via EW alone.

This can be rationalized with our approximate calculations, which indicate that the pinning and EW forces are of comparable magnitude. This limitation is, however, not inherent. It could be overcome via an improved design of the electrode geometry.

In the current design, only three electrode connections were used to create multiple trapping and release stations. This is efficient, but also poses limitations to the EW force. Use of individually addressable electrode pairs (see Fig. 6d) per trapping and release geometry would take away this limitation.

Our device should be well suited for studies of cells in droplets (or cell supernatants) with SPRi, where it is desirable to perform multiplex analysis of the same droplet on subsequent sensor patches, and to reuse the chip after replacement of either actuation or detector surface. Exchange of  $\text{O}_2$  and  $\text{CO}_2$  produced by the cell during this time is favored by the relatively large amount of oil surrounding the drops. Enhancement of the throughput could be achieved via parallelization, i.e., the use of multiple traps side by side. This is straightforward to accomplish, as we have previously shown in de Ruiter et al. (2014), where droplets were laterally guided and trapped atop multiple arrays of electrodes. This principle can be adapted for the use of multiple trapping and release geometries as well.

**Acknowledgments** This research was supported by the Dutch Technology Foundation STW, which is part of the Netherlands Organization for Scientific Research (NWO) and which is partly funded by the Ministry of Economic Affairs.

**Open Access** This article is distributed under the terms of the Creative Commons Attribution 4.0 International License (<http://creativecommons.org/licenses/by/4.0/>), which permits unrestricted use, distribution, and reproduction in any medium, provided you give appropriate credit to the original author(s) and the source, provide a link to the Creative Commons license, and indicate if changes were made.

## References

- Baret JC, Mugele F (2006) Electrical discharge in capillary breakup: controlling the charge of a droplet. *Phys Rev Lett* 96:016106. doi:10.1103/PhysRevLett.96.016106
- Baret JC et al (2009) Fluorescence-activated droplet sorting (FADS): efficient microfluidic cell sorting based on enzymatic activity. *Lab Chip* 9:1850–1858. doi:10.1039/b902504a
- Bithi SS, Wang WS, Sun M, Blawdziewicz J, Vanapalli SA (2014) Coalescing drops in microfluidic parking networks: a multifunctional platform for drop-based microfluidics. *Biomicrofluidics* 8:034118. doi:10.1063/1.4885079
- Calvert P (2001) Inkjet printing for materials and devices. *Chem Mater* 13:3299–3305. doi:10.1021/cm0101632
- Casadevall i Solvas X, deMello A (2011) Droplet microfluidics: recent developments and future applications. *Chem Commun* 47:1936–1942. doi:10.1039/C0CC02474K

- Cavalli A, Musterd M, Mugele F (2015) Numerical investigation of dynamic effects for sliding drops on wetting defects. *Phys Rev E* 91:023013. doi:[10.1103/PhysRevE.91.023013](https://doi.org/10.1103/PhysRevE.91.023013)
- Chabert M, Viovy JL (2008) Microfluidic high-throughput encapsulation and hydrodynamic self-sorting of single cells. *Proc Natl Acad Sci USA* 105:3191–3196. doi:[10.1073/pnas.0708321105](https://doi.org/10.1073/pnas.0708321105)
- Chen JS, Jiang JH (2012) Droplet microfluidic technology: microdroplets formation and manipulation. *Chin J Anal Chem* 40:1293–1300. doi:[10.1016/S1872-2040\(11\)60567-7](https://doi.org/10.1016/S1872-2040(11)60567-7)
- Cho SK, Moon HJ, Kim CJ (2003) Creating, transporting, cutting, and merging liquid droplets by electrowetting-based actuation for digital microfluidic circuits. *J Microelectromech S* 12:70–80. doi:[10.1109/Jmems.2002.807467](https://doi.org/10.1109/Jmems.2002.807467)
- de Ruiter R, Pit AM, de Oliveira VM, Duits MHG, van den Ende D, Mugele F (2014) Electrostatic potential wells for on-demand drop manipulation in microchannels. *Lab Chip*. doi:[10.1039/c3lc51121a](https://doi.org/10.1039/c3lc51121a)
- Erickson D, Mandal S, Yang AHJ, Cordovez B (2008) Nanobiosensors: optofluidic, electrical and mechanical approaches to biomolecular detection at the nanoscale. *Microfluid Nanofluid* 4:33–52. doi:[10.1007/s10404-007-0198-8](https://doi.org/10.1007/s10404-007-0198-8)
- Fradet E, McDougall C, Abbyad P, Dangla R, McGloin D, Baroud CN (2011) Combining rails and anchors with laser forcing for selective manipulation within 2D droplet arrays. *Lab Chip* 11:4228–4234. doi:[10.1039/c1lc20541b](https://doi.org/10.1039/c1lc20541b)
- Gu H, Murade CU, Duits MHG, Mugele F (2011) A microfluidic platform for on-demand formation and merging of microdroplets using electric control. *Biomicrofluidics* 5:011101. doi:[10.1063/1.3570666](https://doi.org/10.1063/1.3570666)
- Guo MT, Rotem A, Heyman JA, Weitz DA (2012) Droplet microfluidics for high-throughput biological assays. *Lab Chip* 12:2146–2155. doi:[10.1039/c2lc21147e](https://doi.org/10.1039/c2lc21147e)
- Kuswandi B, Nuriman Huskens J, Verboom W (2007) Optical sensing systems for microfluidic devices: a review. *Anal Chim Acta* 601:141–155. doi:[10.1016/j.aca.2007.08.046](https://doi.org/10.1016/j.aca.2007.08.046)
- Leung K et al (2012) A programmable droplet-based microfluidic device applied to multiparameter analysis of single microbes and microbial communities. *Proc Natl Acad Sci USA* 109:7665–7670. doi:[10.1073/pnas.1106752109](https://doi.org/10.1073/pnas.1106752109)
- Li F, Mugele F (2008) How to make sticky surfaces slippery: contact angle hysteresis in electrowetting with alternating voltage. *Appl Phys Lett* 92:244108. doi:[10.1063/1.2945803](https://doi.org/10.1063/1.2945803)
- Luo Y, Yu F, Zare RN (2008) Microfluidic device for immunoassays based on surface plasmon resonance imaging. *Lab Chip* 8:694–700. doi:[10.1039/b800606g](https://doi.org/10.1039/b800606g)
- Mairhofer J, Roppert K, Ertl P (2009) Microfluidic systems for pathogen sensing. *A Rev Sensors* 9:4804–4823. doi:[10.3390/s90604804](https://doi.org/10.3390/s90604804)
- Malic L, Veres T, Tabrizian M (2009) Two-dimensional droplet-based surface plasmon resonance imaging using electrowetting-on-dielectric microfluidics. *Lab Chip* 9:473–475. doi:[10.1039/b814697g](https://doi.org/10.1039/b814697g)
- Malic L, Veres T, Tabrizian M (2011) Nanostructured digital microfluidics for enhanced surface plasmon resonance imaging. *Biosens Bioelectron* 26:2053–2059. doi:[10.1016/j.bios.2010.09.001](https://doi.org/10.1016/j.bios.2010.09.001)
- Margulies M et al (2005) Genome sequencing in microfabricated high-density picolitre reactors. *Nature* 437:376–380. doi:[10.1038/nature03959](https://doi.org/10.1038/nature03959)
- Mugele F, Baret J-C (2005) Electrowetting: from basics to applications. *J Phys: Condens Matter* 17:R705. doi:[10.1088/0953-8984/17/28/R01](https://doi.org/10.1088/0953-8984/17/28/R01)
- Nisisako T, Torii T (2008) Microfluidic large-scale integration on a chip for mass production of monodisperse droplets and particles. *Lab Chip* 8:287–293. doi:[10.1039/b713141k](https://doi.org/10.1039/b713141k)
- Pit AM, de Ruiter R, Kumar A, Wijnperle D, Duits MH, Mugele F (2015a) High-throughput sorting of drops in microfluidic chips using electric capacitance. *Biomicrofluidics* 9:044116. doi:[10.1063/1.4928452](https://doi.org/10.1063/1.4928452)
- Pit AM, Duits MHG, Mugele F (2015b) Droplet manipulations in two phase flow microfluidics. *Micromachines* 6:1768–1793. doi:[10.3390/mi6111455](https://doi.org/10.3390/mi6111455)
- Rich RL, Myszkowski DG (2007) Higher-throughput, label-free, real-time molecular interaction analysis. *Anal Biochem* 361:1–6. doi:[10.1016/j.ab.2006.10.040](https://doi.org/10.1016/j.ab.2006.10.040)
- Schmid L, Weitz DA, Franke T (2014) Sorting drops and cells with acoustics: acoustic microfluidic fluorescence-activated cell sorter. *Lab Chip* 14:3710–3718. doi:[10.1039/c4lc00588k](https://doi.org/10.1039/c4lc00588k)
- Schoeman RM, Kemna EW, Wolbers F, van den Berg A (2014) High-throughput deterministic single-cell encapsulation and droplet pairing, fusion, and shrinkage in a single microfluidic device. *Electrophoresis* 35:385–392. doi:[10.1002/elps.201300179](https://doi.org/10.1002/elps.201300179)
- Seemann R, Brinkmann M, Pfohl T, Herminghaus S (2012) Droplet based microfluidics. *Rep Prog Phys* 75:016601. doi:[10.1088/0034-4885/75/1/016601](https://doi.org/10.1088/0034-4885/75/1/016601)
- Song H, Chen DL, Ismagilov RF (2006) Reactions in droplets in microfluidic channels. *Angew Chem* 45:7336–7356. doi:[10.1002/anie.200601554](https://doi.org/10.1002/anie.200601554)
- Staicu A, Mugele F (2006) Electrowetting-induced oil film entrapment and instability. *Phys Rev Lett* 97:167801. doi:[10.1103/PhysRevLett.97.167801](https://doi.org/10.1103/PhysRevLett.97.167801)
- Stojanovic I, Schasfoort RB, Terstappen LW (2014) Analysis of cell surface antigens by Surface Plasmon Resonance imaging. *Biosens Bioelectron* 52:36–43. doi:[10.1016/j.bios.2013.08.027](https://doi.org/10.1016/j.bios.2013.08.027)
- Stojanovic I, van der Velden TJ, Mulder HW, Schasfoort RB, Terstappen LW (2015) Quantification of antibody production of individual hybridoma cells by surface plasmon resonance imaging. *Anal Biochem* 485:112–118. doi:[10.1016/j.ab.2015.06.018](https://doi.org/10.1016/j.ab.2015.06.018)
- t Mannetje D, Banpurkar A, Koppelman H, Duits MH, van den Ende D, Mugele F (2013) Electrically tunable wetting defects characterized by a simple capillary force sensor. *LangmuirACS J Surfaces Colloids* 29:9944–9949. doi:[10.1021/la4015724](https://doi.org/10.1021/la4015724)
- t Mannetje D et al (2014) Trapping of drops by wetting defects. *Nat Commun* 5:3559. doi:[10.1038/ncomms4559](https://doi.org/10.1038/ncomms4559)
- Takinoue M, Takeuchi S (2011) Droplet microfluidics for the study of artificial cells. *Anal Bioanal Chem* 400:1705–1716. doi:[10.1007/s00216-011-4984-5](https://doi.org/10.1007/s00216-011-4984-5)
- Theberge AB, Courtois F, Schaerli Y, Fischlechner M, Abell C, Hollfelder F, Huck WTS (2010) Microdroplets in microfluidics: an evolving platform for discoveries in chemistry and biology. *Chem Int Edit* 49:5846–5868. doi:[10.1002/anie.200906653](https://doi.org/10.1002/anie.200906653)
- Yeatman EM (1996) Resolution and sensitivity in surface plasmon microscopy and sensing. *Biosens Bioelectron* 11:635–649. doi:[10.1016/0956-5663\(96\)83298-2](https://doi.org/10.1016/0956-5663(96)83298-2)